Monthly Notices
of the
ROYAL ASTRONOMICAL SOCIETY

MNRAS **488,** 3195–3210 (2019)
Advance Access publication 2019 July 8

doi:10.1093/mnras/stz1857

Multiphase gas in the circumgalactic medium: relative role of $t_{\rm cool}/t_{\rm ff}$ and density fluctuations

Prakriti Pal Choudhury,[1,2]★ Prateek Sharma [3] and Eliot Quataert [4]

[1]*Department of Physics, Indian Institute of Science, Bangalore 560012, India*
[2]*Max Planck Institute for Astrophysics, Garching 85748, Germany*
[3]*Department of Physics and Joint Astronomy Program, Indian Institute of Science, Bangalore 560012, India*
[4]*Astronomy Department, Theoretical Astrophysics Center, University of California Berkeley, Berkeley, CA 94720, USA*

Accepted 2019 July 3. Received 2019 July 3; in original form 2019 January 9

ABSTRACT

We perform a suite of simulations with realistic gravity and thermal balance in shells to quantify the role of the ratio of cooling time to the free-fall time ($t_{\rm cool}/t_{\rm ff}$) and the amplitude of density perturbations ($\delta\rho/\rho$) in the production of multiphase gas in the circumgalactic medium (CGM). Previous idealized simulations, focusing on small amplitude perturbations in the intracluster medium (ICM), found that cold gas can condense out of the hot ICM in global thermal balance when the background $t_{\rm cool}/t_{\rm ff} \lesssim 10$. Recent observations suggest the presence of cold gas even when the background profiles have somewhat large values of $t_{\rm cool}/t_{\rm ff}$. This partly motivates a better understanding of additional factors such as large density perturbations that can enhance the propensity for cooling and condensation even when the background $t_{\rm cool}/t_{\rm ff}$ is high. Such large density contrasts can be seeded by galaxy wakes or dense cosmological filaments. From our simulations, we introduce a condensation curve in the $(\delta\rho/\rho) - \min(t_{\rm cool}/t_{\rm ff})$ space, which defines the threshold for condensation of multiphase gas in the CGM. We show that this condensation curve corresponds to $(t_{\rm cool}/t_{\rm ff})_{\rm blob} \lesssim 10$ applied to the overdense blob instead of the background for which $t_{\rm cool}/t_{\rm ff}$ can be higher. We also study the modification in the condensation curve by varying entropy stratification. Steeper (positive) entropy gradients shift the condensation curve to higher amplitudes of perturbations (i.e. make condensation difficult). A constant entropy core, applicable to the CGM in smaller haloes, shows condensation over a larger range of radii as compared to the steeper entropy profiles in the ICM.

Key words: galaxies: clusters: intracluster medium – galaxies: haloes.

1 INTRODUCTION

The origin and fate of cold gas ($\lesssim 10^4$ K) in dark matter haloes is crucial to our understanding of galaxy formation because it provides fuel for star formation, gets expelled by winds/jets, and gets recycled into stars (Tumlinson, Peeples & Werk 2017). Observations of quasar absorption lines and Ly α emission (Rauch & Haehnelt 2011; Matejek & Simcoe 2012; Bowen et al. 2016) suggest that cold gas pervades the circumgalactic medium (CGM) around galaxies within $\lesssim$100 kpc, at different redshifts. Existing theories predict that massive dark matter haloes contain hot, virialized gas in approximate hydrostatic equilibrium (Birnboim & Dekel 2003). Only the haloes less massive than $3 \times 10^{11}\,{\rm M}_\odot$ are expected to have narrow cold cosmological filaments directly feeding the central galaxies (Dekel et al. 2009). Hence, the origin of the diffuse multiphase gas along almost all lines of sight in the CGM is not well understood.

On the other hand, emission line filaments and molecular gas are present in the cores ($\lesssim$few 10s of kpc) of galaxy clusters and groups at low redshifts (Cavagnolo et al. 2009; O'Sullivan et al. 2017). In the absence of cooling flow signatures in galaxy clusters, it is presumed that feedback from the central supermassive black hole predominantly helps in maintaining thermal balance in the cores (Fabian 1994). While local thermal instability (TI) is a viable mechanism that can generate dense filaments in the intracluster medium (ICM; Field 1965; Balbus 1988; Nulsen 1997), there is no consensus on the origin of cold gas in the CGM. In this work, we perform idealized simulations to explore the relative roles of different physical parameters important for the condensation in the ICM/CGM. Additionally, we investigate if the physical principles, applicable to understand the formation of cold gas in the ICM, can be consistently generalized in the context of the CGM.

★ E-mail: prakritic@iisc.ac.in

The formation of cold gas via local TI and its relation to cluster observables have been the focus of observations as well as simulations of galaxy clusters (Salomé et al. 2006; Sharma, Parrish & Quataert 2010; McCourt et al. 2012; Tremblay et al. 2012; Voit et al. 2015a; Tremblay et al. 2016). According to the models built on this idea, these cold clumps provide fuel for the central black hole and feedback jets that maintain thermal balance, thus completing the feedback cycle (Pizzolato & Soker 2005; Li & Bryan 2014; Prasad, Sharma & Babul 2015; Voit et al. 2015b). Earlier simulations have shown that condensation due to local TI is triggered only when the background ICM has the minimum ratio of the cooling time to the free-fall time ($t_{\rm cool}/t_{\rm ff}$) below $\sim$10 for realistic cool cluster cores (McCourt et al. 2012; Sharma et al. 2012a).

Recently Meece, O'Shea & Voit (2015) claimed, based on their idealized simulations, that cold gas can condense out even if the ratio of the cooling time to the free-fall time is larger than 10. Following that, Choudhury & Sharma (2016), using global linear stability analysis and idealized simulations, explored the possibility of higher threshold values of the ratio by considering idealized potentials, somewhat different from the NFW (Navarro, Frenk & White 1996) potential typically considered in clusters. These studies also find that the $t_{\rm cool}/t_{\rm ff}$ threshold lies around 10 (within at most a factor of 2) for realistic clusters, as long as the density perturbations ($\delta\rho/\rho$) are small ($\lesssim$1).

Hogan et al. (2017) recently observed the profiles of 56 clusters from *Chandra* X-ray observatory (33 of which are cool cores with H α emission) and deduced that almost all of these have $\min(t_{\rm cool}/t_{\rm ff}) \gtrsim 10$. A larger sample from Pulido et al. (2018) shows some cores with $\min(t_{\rm cool}/t_{\rm ff}) < 10$, but discrepancies between observations and simulations remain (see section 4.4 of Pulido et al. 2018 for a detailed discussion; see also section 4.1 of Prasad, Sharma & Babul 2018). This raises doubts on TI models and gives impetus to understand multiphase condensation with large $t_{\rm cool}/t_{\rm ff}$.

It is anticipated that large density perturbations make it easy for condensation to occur (Pizzolato & Soker 2005; Singh & Sharma 2015). In this paper, we set up extensive numerical experiments to explore the role of density perturbations in multiphase condensation. We begin with a hydrostatic ICM, confined by the NFW potential (and additionally BCG potential in some cases) and defined by a radially varying entropy profile, identical to what is described in Choudhury & Sharma (2016). We introduce large, isobaric density inhomogeneities in some of the background profiles. The main motivation of our work is to understand how the initial background $t_{\rm cool}/t_{\rm ff}$ and amplitudes of density perturbations, $\delta\rho/\rho$, govern the condensation of multiphase gas in the ICM. Earlier idealized simulations, which found $\min(t_{\rm cool}/t_{\rm ff}) \approx 10$ threshold to be robust in the cluster–gravity regime, focused only on low-amplitude perturbations ($\delta\rho/\rho$).

We scan the range of the two key parameters [($\delta\rho/\rho$)–$\min(t_{\rm cool}/t_{\rm ff})$] to delineate the space in which multiphase condensation occurs. We find that large background $t_{\rm cool}/t_{\rm ff}$ requires a large initial perturbation for cold gas to condense out. Large density perturbations may explain the cold gas in clusters of significantly high background $\min(t_{\rm cool}/t_{\rm ff})$ than the threshold value of 10. However, we see that the condensation curve roughly traces out the locus of $t_{\rm cool}/t_{\rm ff} \lesssim 10$ for a small overdensity seeded in the background medium. For large amplitudes of perturbations, the effective $t_{\rm cool}/t_{\rm ff}$ of the overdense blob has to fall below a threshold to obtain multiphase condensation in a background medium having a significantly large $t_{\rm cool}/t_{\rm ff}$.

Radio and X-ray observations show large-scale, low-density cavities that are the relics of jet events in cool-core clusters. The trails of these high-speed jets can contain tiny regions, roughly at the same pressure with the surroundings, but with a larger local density than that of the background. Larger density perturbations are also expected for lower mass CGM where feedback is expected to cause a larger deviation from hydrostatic equilibrium (Fielding et al. 2017; Oppenheimer 2018). Cold mode accretion along cosmological filaments can generate large overdensities as well (Kereš & Hernquist 2009). We mimic such large density enhancements in the ICM by putting large-amplitude, isobaric density perturbations in our idealized model. We also test the robustness of our condensation curve for various scenarios such as localized perturbations, rising buoyant bubbles, jets, and different entropy stratification.

Voit et al. (2017) argued that the role of the radial entropy gradient in the ICM is understated and it primarily regulates the stochastic cold accretion and feedback cycles. So, we study the effects of entropy variation on the condensation curve by using different initial entropy profiles. We find that the presence of the internal gravity waves with a positive entropy gradient does make condensation difficult, requiring moderately lower values of $\min(t_{\rm cool}/t_{\rm ff})$ for condensation. On the other hand, with a constant entropy in which internal gravity waves are absent, it is only slightly easier to condense. Thus, just the linear response may not predict cold gas condensation very accurately. However, we find disrupted large cores and relatively enhanced cold gas in a constant entropy medium, once condensation is triggered. This flatter entropy profile (large core) is probably more relevant for lower mass haloes (such as Milky Way) in contrast to clusters.

In Section 2, we describe the set-up and relevant details of initialization of the virialized ICM. Section 3 shows the results. We discuss the astrophysical implications of our results in Section 4. We conclude in Section 5.

2 PHYSICAL/SIMULATION SET-UP

2.1 Model and equations

We model the initial background ICM to be in hydrostatic and thermal equilibrium. The following equations describe the evolution of the gas:

$$\frac{{\rm D}\rho}{{\rm D}t} = -\rho\nabla\cdot v + S_\rho, \tag{1}$$

$$\frac{{\rm D}v}{{\rm D}t} = -\frac{1}{\rho}\nabla p - g\hat{r} + \frac{1}{\rho}S_\rho v_{\rm jet}\hat{r}, \tag{2}$$

$$\frac{p}{(\gamma-1)}\frac{\rm D}{{\rm D}t}\left[\ln\left(\frac{p}{\rho^\gamma}\right)\right] = -q^-(n,T) + q^+(r,t), \tag{3}$$

where D/Dt is the Lagrangian derivative, ρ, v, and p are the mass density, the velocity, and the pressure; $\gamma = 5/3$ is the adiabatic index; $q^-(n, T) \equiv n_{\rm e} n_i \Lambda(T)$ ($n_{\rm e} \equiv \rho/[\mu_{\rm e} m_{\rm p}]$ and $n_i \equiv \rho/[\mu_i m_{\rm p}]$ are the electron and the ion number densities, respectively; $\mu_{\rm e} = 1.17$, $\mu_i = 1.32$, and $m_{\rm p}$ is the proton mass) and $q^+(r, t) \equiv \langle q^-\rangle$ (which imposes thermal balance in shells), $\Lambda(T)$ is the temperature-dependent cooling function. We use a fit to the plasma cooling function with a third of the solar metallicity, given by equation (12) and the solid line in fig. 1 of Sharma et al. (2010). Thus, the set-up is very similar to Sharma et al. (2012a), the main difference being large-density perturbations. In some runs, we inject kinetic jets of constant power with jet mass and momentum source terms that we describe in Section 2.3.6.

2.1.1 Gravitational potential

For some of our runs, we use the standard NFW (Navarro, Frenk & White 1996) gravitational potential as given by equations (4) and (5) of Choudhury & Sharma (2016). For some runs, we add a BCG potential to the NFW potential, of the following form:

$$\Phi_{\rm BCG} = {V_c}^2 \ln(r/r_0), \tag{4}$$

where $V_c = 350\,{\rm km\,s^{-1}}$ and $r_0 = 1$ kpc. This accounts for the gravity due to the central galaxy that typically dominates within $\sim$10 kpc.

2.1.2 Equilibrium profile

We have a background hydrostatic equilibrium that implies ${\rm d}p_0/{\rm d}r = -\rho_0 g$, where a subscript '0' refers to equilibrium quantities and the acceleration due to gravity $g \equiv {\rm d}\Phi/{\rm d}r$ (Φ is the fixed gravitational potential). The entropy profile of the ICM in initial hydrostatic equilibrium is specified as (Cavagnolo et al. 2009)

$$K(r) = \frac{T_{\rm keV}}{n_{\rm e}^{\gamma-1}} = K_0 + K_{100}\left(\frac{r}{r_{100}}\right)^{\alpha}, \tag{5}$$

where $r_{100} = 100$ kpc. We vary K_0 to obtain background profiles with different $t_{\rm cool}/t_{\rm ff}$. There are runs in which we study the effect of entropy variation. For these cases, we either have $K_0 = 0$ or $K_{100} = 0$, and hence vary the non-zero parameter. Additionally, we have runs in which we vary α to obtain a stronger entropy stratification.

2.1.3 Important time-scales

The TI time-scale (the inverse of the local exponential growth rate for a constant heating rate per unit volume) is relevant for the isobaric modes and is given by

$$t_{\rm TI} = \frac{\gamma t_{\rm cool}}{(2 - {\rm d}\ln\Lambda/{\rm d}\ln T)}, \tag{6}$$

where

$$t_{\rm cool} = \frac{nk_{\rm B}T}{(\gamma-1)n_{\rm e}n_i\Lambda}. \tag{7}$$

We use $\min(t_{\rm cool}/t_{\rm ff})$ and $\min(t_{\rm TI}/t_{\rm ff})$ interchangeably as the values are almost equal for clusters. For only free–free cooling (with $\Lambda \propto T^{\frac{1}{2}}$) relevant to clusters, $t_{\rm TI} = (10/9)t_{\rm cool}$ but it may differ in other cases. The free-fall time

$$t_{\rm ff} = \left(\frac{2r}{g}\right)^{1/2}, \tag{8}$$

where $g(r)$ is the gravitational acceleration at the radius of interest.

2.2 Simulation set-up

We use the ZEUS-MP code (Hayes et al. 2006) to solve Euler equations with source terms such as heating, cooling, and gravity (equations 1–3). The initial condition consists of a hydrostatic equilibrium profile (described in Section 2.1), superposed with isobaric density perturbations.

2.2.1 Grids and geometry

All the simulations are done in spherical (r, θ, ϕ) coordinates with a resolution 256×256 ($N_r \times N_\theta$). The radial grid in spherical runs is logarithmic, with an equal number of grid points from 1 to 10 kpc and 10 to 100 kpc. We had to perform hundreds of simulations to map out the condensation curve in the $(\delta - t_{\rm TI}/t_{\rm ff})$ space and hence 3D simulations are prohibitively expensive.

2.2.2 Initial and boundary conditions

We seed isobaric density perturbations (equivalently, entropy perturbations) described in section 4.1.2 of Choudhury & Sharma (2016), except that we vary the amplitudes in this work. We label our runs with the maximum value of overdensity δ, where

$$\delta(r,\theta,\phi) = \frac{\rho(r,\theta,\phi) - \bar{\rho}(r)}{\bar{\rho}(r)} \tag{9}$$

and $\bar{\rho}$ denotes the shell-averaged quantity. The overdensity field is identical for all the runs and we simply scale the amplitude for different simulations. The overdensity field is expressed as a sum over Fourier modes in a Cartesian basis and therefore its shell-averaged value is non-zero. We use $\delta_{\rm max}$ and $\delta_{\rm rms}(r)$ in this work extensively to denote the maximum value of δ over the entire simulation box and the root-mean-square δ in each shell, respectively.

At the outer boundary, the electron number density is fixed to be $n_{\rm e,out} = 0.00875\,{\rm cm^{-3}}$ for most of the runs. For the runs with a constant initial entropy (and the runs presented in Section 3.3.1) the value is $n_{\rm e,out} = 0.035\,{\rm cm^{-3}}$. In this case, we start with higher densities in general because simulations with higher outer densities are better behaved numerically.[1] We perform appropriate comparisons of these runs having high outer densities with the standard runs to verify the robustness of our results. All these runs with higher $n_{\rm e,out}$ show threshold $t_{\rm TI}/t_{\rm ff}$ for condensation, which are consistent with the condensation curve.

The boundary conditions in the radial direction allow outflow at the inner boundary ($r_{\rm in} = 1$ kpc) and inflow at the outer boundary ($r_{\rm out} = 100$ kpc), with the density and internal energy density fixed to their initial equilibrium values at the outer boundary. The boundary conditions for θ ($0 < \theta \leq \pi$) and ϕ ($0 < \phi \leq 2\pi$) directions are, respectively, reflective/axisymmetric and periodic.

2.2.3 Initial negative density

We investigate the effects of very large ($\delta > 1.0$) amplitude density perturbations in the ICM and while doing so, we find that some grid points develop negative density at $t = 0$. To solve this problem and to keep the mean background density profile unaltered, we do the following. We add a floor density at the points with negative density. We keep track of the gas mass added in a shell and then subtract the shell-averaged density added from the densities at all points in the shell. We do this for each radial shell and thus the background density profile remains unchanged. Mathematically,

$$\rho_{\rm sub} = \frac{\int_{A_{\rm neg}} (\rho_{\rm floor} - \rho_{\rm nd}) r^2 \sin\theta {\rm d}\theta {\rm d}\phi}{\int_A r^2 \sin\theta {\rm d}\theta {\rm d}\phi}, \tag{10}$$

where $\rho_{\rm nd}$ denotes the density at the grid points where it becomes negative, $A_{\rm neg}$ implies that the integral in the numerator is carried out over the grid points with negative densities in a given shell, $\rho_{\rm sub}$

[1] We observe spurious features emerging at the outer boundary for the constant entropy runs with a lower outer density. We do not quite understand the origin of these features, but these are absent for a higher outer density. By visual inspection of density snapshots, we ensure that such artificial features are absent in all our runs.

Table 1. Numerical experiments to quantify the relative role of $\min(t_{\rm TI}/t_{\rm ff})$ and δ.

Gravity	Density perturbations	Parameters varied	Additional factors
NFW	Throughout medium	K_0, δ	–
NFW + BCG	Throughout medium	K_0, δ	–
NFW + BCG	Localized shell	K_0, δ	–
NFW + BCG	Throughout medium	K_0, δ, $K_{100} = 0$	–
NFW + BCG	Throughout medium	K_{100}, δ, α, $K_0 = 0$	–
NFW + BCG	Throughout medium	K_0, δ, $\dot{M}_{\rm acc}$	AGN jet
NFW + BCG	Throughout medium	K_0, δ	Bubble

Note. Each of the cases has multiple runs with different values of the parameters.

is the density that should be calculated and subtracted for each grid point in the shell, and the integral in the denominator is carried out over all the grid points in the shell.

2.3 Numerical experiments

In this section, we briefly describe the various numerical experiments that we carry out to quantify the relative role of background $\min(t_{\rm cool}/t_{\rm ff})$ and density perturbations in multiphase condensation. Table 1 shows all the numerical experiments concisely.

2.3.1 NFW potential with different perturbations

For this set-up, our gravitational potential is only due to the dark matter halo. The initial background density and cooling time are fixed by the entropy parameters K_0 (see Section 2.1.2). Fig. 1 shows the typical initial conditions for this set-up. For different background profiles (with different $\min(t_{\rm cool}/t_{\rm ff})$), we initialize the ICM with different amplitudes of perturbations to map out the regime in which multiphase condensation happens. The runs with low-amplitude perturbations ($\delta \lesssim 1$) result in the standard $\min(t_{\rm cool}/t_{\rm ff}) \lesssim 10$ criterion that was explored most recently in Choudhury & Sharma (2016). For large perturbations ($\delta \gtrsim 1$), we ensure that the lowest density regions do not have negative values (see Section 2.2.3).

2.3.2 NFW + BCG potential with different perturbations

For these runs, the potential is due to the dark matter as well as the central galaxy (Section 2.1.1). Recent works (Voit & Donahue 2015; Hogan et al. 2017; Prasad et al. 2018) have highlighted the importance of including the BCG gravity in cool-core clusters. Here, the initialization is done exactly like in Section 2.3.1. With the free-fall time shorter due to additional gravity, to get a similar $\min(t_{\rm cool}/t_{\rm ff})$, for these runs we require the cooling times to be lower (or K_0 smaller) compared to the NFW-only regime.

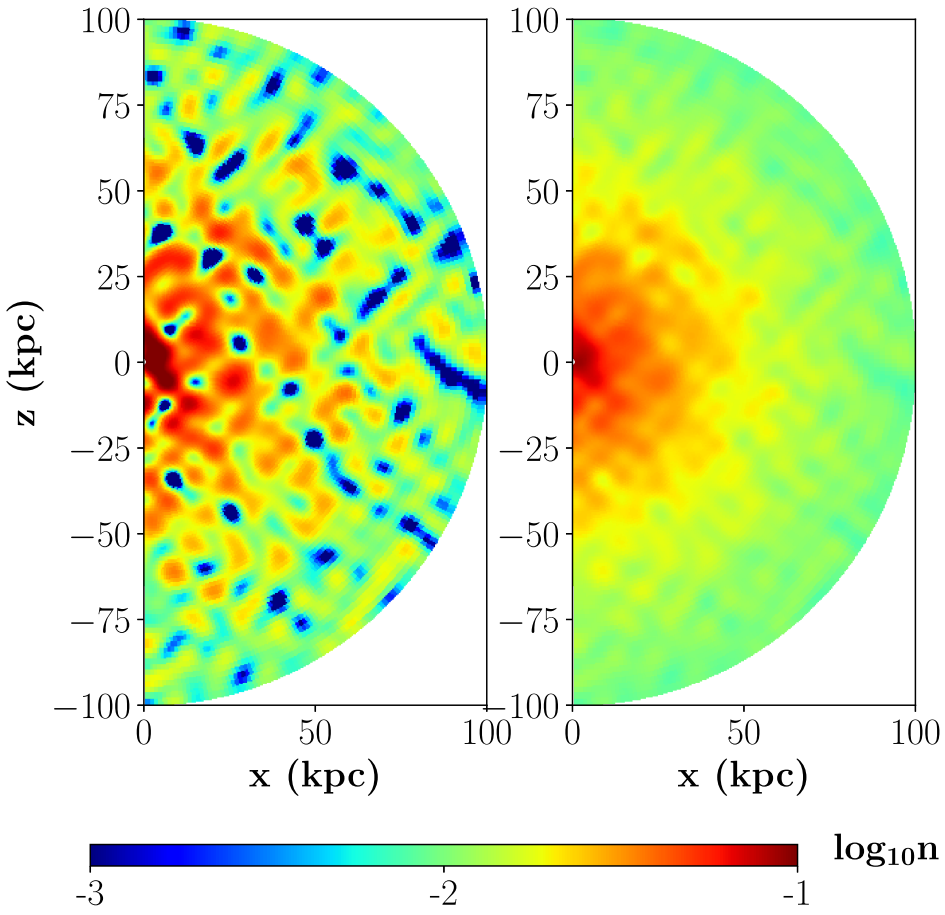

Figure 1. The initial number density snapshots for fiducial runs with only NFW gravity ($K_0 = 8$ keV cm^2) and with large (left) and small (right) amplitudes of density perturbations ($\delta_{\rm max} \approx 1.6$ and 0.32, respectively). The colour bar is clipped at the maximum and minimum values such that the density larger (smaller) than 0.1 (10^{-3}) cm^{-3} corresponds to the reddest (bluest) colour.

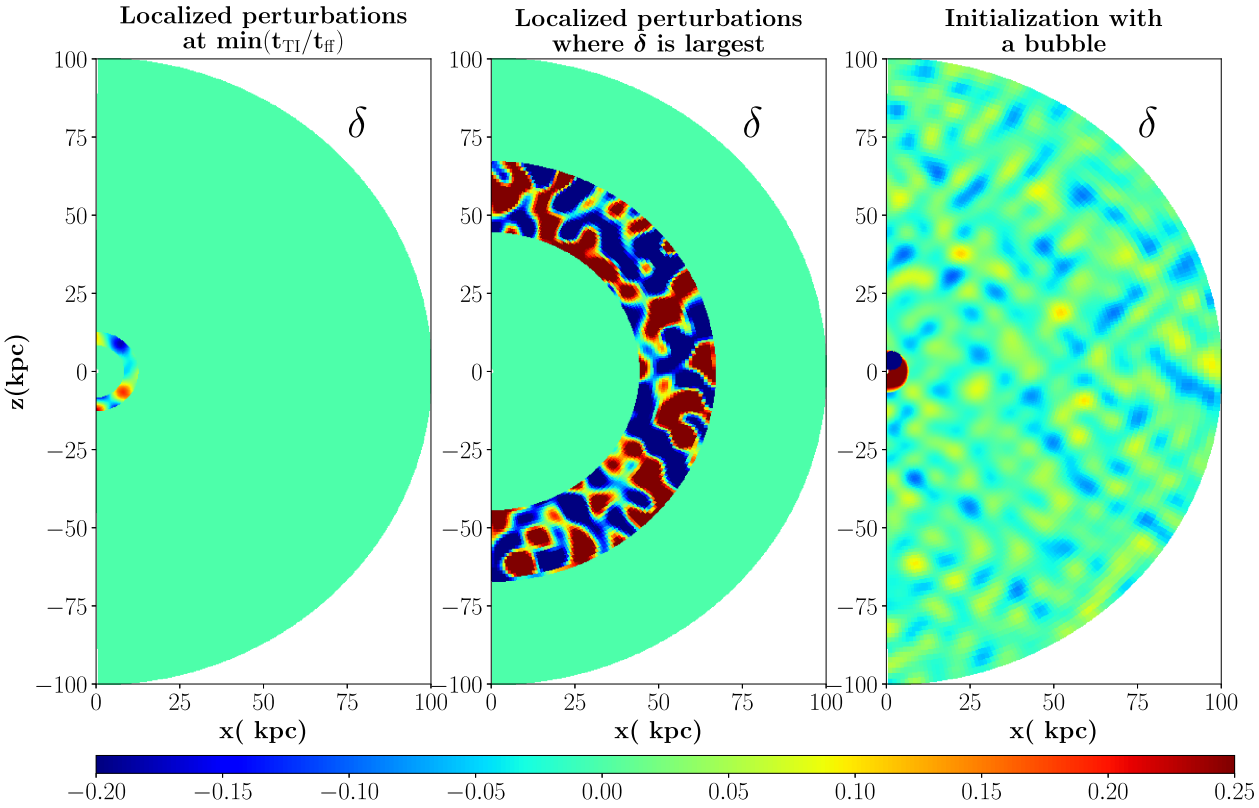

Figure 2. The initial overdensity (δ) for the two cases with localized perturbations (left two panels) and a low-density bubble (right-hand panel) in the ICM with the NFW + BCG potential and the background entropy parameter $K_0 = 5$ keV cm^2 corresponding to $\min(t_{\rm TI}/t_{\rm ff}) = 8.18$. In the third panel, there is apparently a dense core at the centre because it shows the density contrast between the background and the bubble.

2.3.3 NFW + BCG potential with localized perturbations

In these simulations, we initialize isobaric perturbations only in a few localized spherical shells, with both high and low amplitudes. We put perturbations within $0.8H_1$ and $1.2H_1$ where H_1 is the radius around which we intend to perturb the medium. We want to explore how the radial location of perturbations can shift the zone of condensation in the $\min(t_{\rm cool}/t_{\rm ff}) - \delta\rho/\rho$ parameter space. The first two panels of Fig. 2 show examples of localized perturbations.

2.3.4 NFW + BCG potential with perturbations and a bubble

In these simulations, we inject a low-density bubble in 2D, of radius 3 kpc and centred at 4 kpc so that it touches the inner boundary, and also perturb the background medium similar to some of the previous set-ups. The bubble has a density of 0.1 times the background. The perturbations are small scale when compared to the spatial extent of the bubble. The bubble will rise buoyantly and it is interesting to understand how that affects multiphase condensation. The third panel in Fig. 2 shows the initialization with a spherical bubble (which is a torus in 3D because of axisymmetry). We also test the results with bubbles centred at 3 and 2 kpc with radius 2 and 1 kpc, respectively. The results are quite similar.

2.3.5 NFW + BCG potential with perturbations and entropy variation

We explore how the entropy gradient affects the susceptibility to condensation. There are two sets of runs for this investigation. The first in which the initial entropy (see Section 2.1.2) is constant throughout the cluster ($K_{100} = 0$) and we vary K_0. In the other set, we have an initial condition with power-law entropy profiles ($K_0 = 0$) in which we vary K_{100} and α.

2.3.6 NFW + BCG potential with perturbations and jet

We inject jets, with mass and radial momentum source terms as in equations (1) and (2), of constant mechanical power and mass-loading into the ICM. The source term consists of $S_\rho \propto \dot{M}_{\rm jet}$ as described by Prasad et al. (2015), where $\dot{M}_{\rm jet}$ is the jet mass-loading factor given by their equation (6) (we use a constant $\dot{M}_{\rm acc}$, 0.01 M$_\odot$/yr and 0.1 M$_\odot$/yr for two sets of runs, unlike Prasad et al. 2015 who calculate $\dot{M}_{\rm acc}$ at $\sim$1 kpc at each time-step). The velocity of the jet is fixed at $\approx 0.2c$ and the jet has an opening angle of 15 deg. The spatial distribution is described by equation (5) of Prasad et al. (2015). Strong jets are usually expected to impinge the medium and create low-density regions surrounded by shells of large densities. Hence, injection of jets can cause higher densities, driving condensation for a short time although they heat up the medium on an average and globally reduce the susceptibility to condensation. In our set-up, we also have cooling and heating balanced in shells. Hence, injection of jets with large powers causes overheating in the medium and prevents condensation. The two cases of jet injection that we try, inject small mechanical powers, 1.5×10^{41} erg s^{-1} (low) and 1.5×10^{42} erg s^{-1} (high). Moreover, the low-energy injection rates also reflect in a gentle subsonic wind in the cluster core instead of a powerful outflow and the jet does not significantly heat the gas. We prefer to keep the thermal balance in the shells to compare the

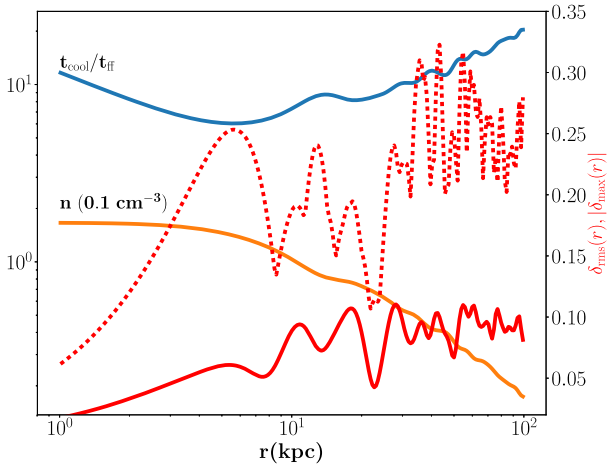

Figure 3. The initial shell-averaged profiles with only NFW gravity ($K_0 = 8$ keV cm^2) and with the amplitude of perturbations $\delta_{max} \approx 0.32$. The secondary y-axis represents the scale for density perturbation amplitudes. The solid red line shows δ_{rms}, the rms perturbation (when averaged across θ-direction; see equation 12) at each radius. The dotted red line shows δ_{max}, the maximum perturbation, at each radius.

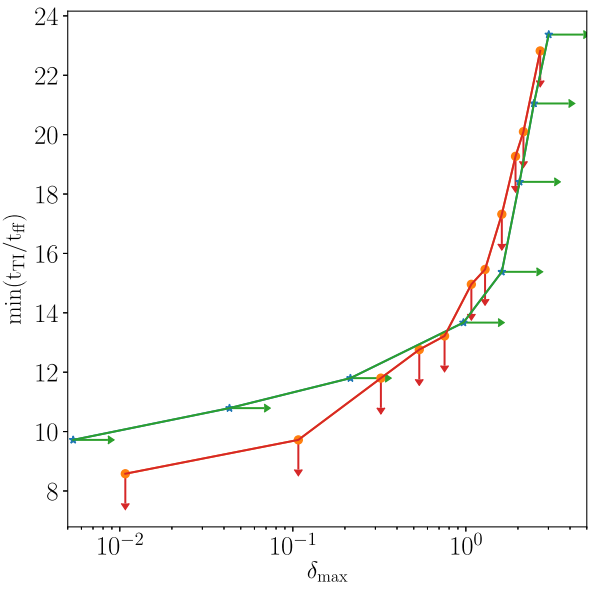

Figure 4. The parameter space for cold gas formation with NFW gravity showing the maximum value of min(t_{TI}/t_{ff}) that shows cold gas condensation for a given amplitude of perturbation (denoted by the vertical down arrows) and the minimum amplitude of density perturbations required for a given background profile and min(t_{TI}/t_{ff}) (denoted by the horizontal right arrows). The two curves may not be identical as in one case the background is changing, while in another the perturbations in the background are changing in amplitude.

results with the rest of the cases and understand the effect of jets in multiphase condensation in a background hydrostatic and thermal balance. Hence, this set-up is not well motivated for jet simulations. Therefore, our jet results should only be considered indicative.

3 RESULTS

We explain our results in this section. All our runs are carried out for a maximum of 15 Gyr.

The most significant aim of this paper is to delineate a condensation zone in the $(\delta\rho/\rho)$ – min(t_{cool}/t_{ff}) space. Note that the min(t_{cool}/t_{ff}) is measured in the unperturbed ICM. The threshold or the boundary of the condensation zone is simply defined by the min(t_{cool}/t_{ff}) or $\delta\rho/\rho$ at which at least some cold gas forms within 15 Gyr. We do not quantify the amount of cold gas formed in detail but we have some comparisons of that for the cases with different entropy profiles (Section 3.3.1). More cold gas is expected the further we go from the threshold line into the condensation zone (Choudhury & Sharma 2016 discuss in more detail how much gas can condense out for different ICM profiles).

To assess the regime of multiphase condensation, we vary the density perturbation amplitude characterized by the maximum value of δ, δ_{max}. Note that δ_{max} is the overdensity at a radius, not equal to the radius of min(t_{cool}/t_{ff}). It provides an appropriate label for the amplitude of perturbations of a medium in which inhomogeneities are seeded throughout the medium.

3.1 NFW

In this section, we build up our condensation curve based on the NFW-only simulations. We perform a series of runs with different amplitudes of initial perturbations for different average t_{cool}/t_{ff} profiles that are set by varying K_0 (see Section 2.1.2). Fig. 3 shows the 1D profile of shell-averaged number density and t_{cool}/t_{ff} for the runs with $\delta_{max} = 0.32$. We have also shown the corresponding root mean square δ (equation 12) and δ_{max} as a function of radius.

3.1.1 *Defining the parameter space*

Fig. 4 shows the condensation curve, to the right/bottom of which there is cold gas formation due to local TI (2.3.1). We have a set of runs in which the amplitude of perturbations (δ_{max}) is fixed and we try to investigate up to what maximum value of min(t_{TI}/t_{ff}) at $t = 0$, we can observe the formation of cold gas by 15 Gyr. The corresponding curve has vertical down arrows showing the region that forms multiphase gas. We have another set in which we fix a background profile with a given value of min(t_{TI}/t_{ff}) for each run and we find out the minimum amplitude of density perturbation that triggers the formation of cold gas. The horizontal right arrows signify the condensation zone. This plot shows that given a large enough amplitude, the background profile with even quite high min(t_{TI}/t_{ff}), can form cold gas.

3.1.2 *Correlation of $\dot{M}$ at the inner boundary and δ_{rms} at min(t_{TI}/t_{ff})*

The crucial question to explore, given a background min(t_{TI}/t_{ff}), is how the core with large perturbations differs from a core with small perturbations. The onset of condensation is expected to be seen within the location of min(t_{cool}/t_{ff}) first and at least a fraction of the cold gas thus formed, is expected to move inwards. So, we expect the mass accretion rate through the inner boundary to shoot up as the gas condenses out. In this section, we investigate how δ_{rms} at min(t_{cool}/t_{ff}) and $\dot{M}$ measured at the inner boundary are correlated.

The left-hand panel in Fig. 5 shows the correlation between accretion across the inner boundary and the density fluctuation (δ_{rms}) at the position of min(t_{TI}/t_{ff}). The red and green solid lines belong to a run with large initial perturbations ($\delta_{max} \approx 1.6$), while the

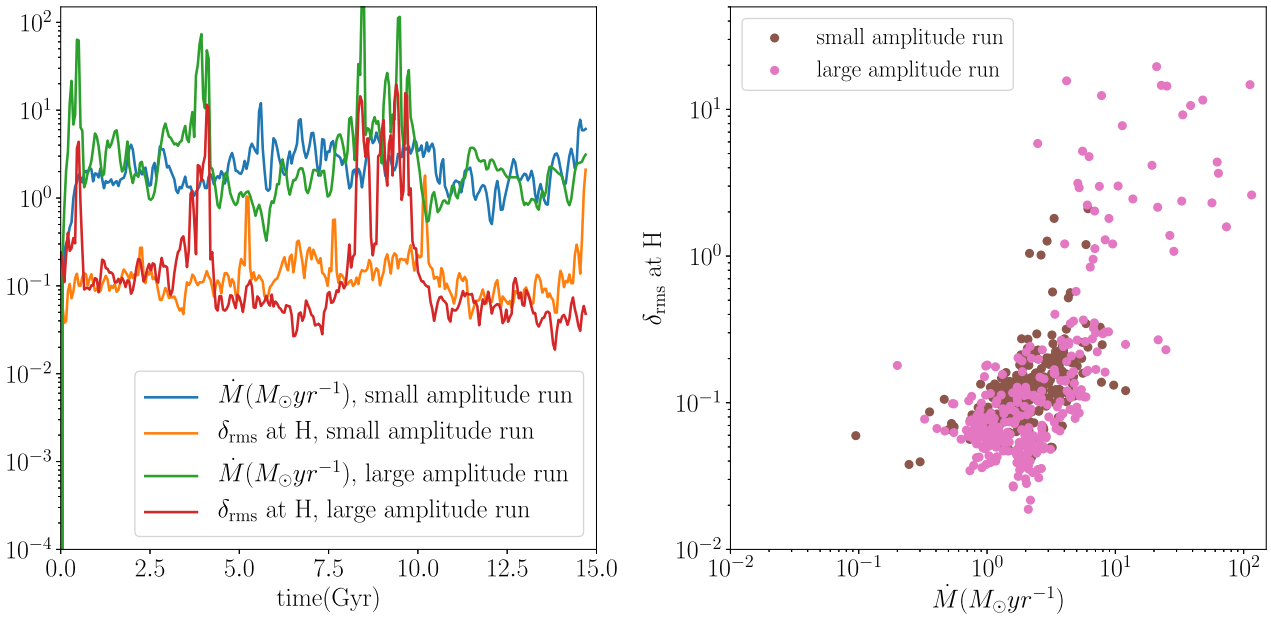

Figure 5. The relation between the mass accretion rate at the inner boundary ($\dot{M}$) and the rms density perturbation amplitude ($\delta_{\rm rms}$) measured at the location (H; averaged between $0.9H$ and $1.1H$) of $\min(t_{\rm TI}/t_{\rm ff})$ for the low ($\delta_{\rm max} = 0.32$) and high ($\delta_{\rm max} = 1.6$) amplitude runs with $K_0 = 8$ keV cm^2 and $K_{100} = 80$ keV cm^2. Left-hand panel: evolution of $\dot{M}$ and $\delta_{\rm rms}$ with time. Right-hand panel: the correlation between $\dot{M}$ and $\delta_{\rm rms}$ at H.

orange and the blue solid lines correspond to a run with small initial perturbations ($\delta_{\rm max} \approx 0.32$) throughout the ICM. We calculate $\dot{M}$ at the inner boundary (r_1) as

$$\dot{M} = \iint {r_1}^2 \rho_1 v_1 \sin(\theta) {\rm d}\theta {\rm d}\phi. \tag{11}$$

The rms amplitude is calculated in the following way:

$$\delta_{\rm rms}(r)^2 = \frac{\iint [(\rho(r,\theta,\phi) - \bar{\rho}(r))/\bar{\rho}(r)]^2 r^2 \sin(\theta) {\rm d}\theta {\rm d}\phi}{\iint r^2 \sin(\theta) {\rm d}\theta {\rm d}\phi}, \tag{12}$$

where $\bar{\rho}(r)$ is shell-averaged density. Now, $\delta_{\rm rms}(r)$ is averaged within $0.9H$ and $1.1H$, where H is the radius of $\min(t_{\rm TI}/t_{\rm ff})$.

It is evident that accretion is highly correlated with $\delta_{\rm rms}$ particularly for a reasonably large $\delta_{\rm rms}$ at H (see right-hand panel of Fig. 5). For smaller perturbations, the density fluctuations growing at $\min(t_{\rm TI}/t_{\rm ff})$ sometimes may not reach the inner boundary and remain suspended within the medium or mix with the hot surroundings before reaching the inner boundary. For the large perturbation amplitude, large cold blobs form and easily decouple from the ICM and hence the correlation is more prominent specifically at large $\delta_{\rm rms}$ (although with a large scatter).

3.2 NFW + BCG: the condensation curve

In this section, we present the condensation curve for the more realistic case of an NFW + BCG potential (see Fig. 6). The presence of BCG reduces the threshold $\min(t_{\rm TI}/t_{\rm ff})$ to some extent for lower amplitudes. But again, with high enough amplitudes, any background profile seems to eventually form cold gas. The underlying red and green lines are for the cases where perturbations are present throughout the medium (following Section 2.3.2). The arrows show the parameter that we vary ($\min[t_{\rm TI}/t_{\rm ff}]$ or $\delta_{\rm max}$) until cold gas is seen, while the other parameter is held fixed.

3.2.1 *Localized perturbations*

As we mention at the beginning of the Section 3, the basic condensation curve is built out of two parameters $\min(t_{\rm TI}/t_{\rm ff})$ and $\delta_{\rm max}$ where the latter denotes the value at the maximum amplitude of the overdensity field. These parameters only label the two variables throughout the domain. The shell-averaged values of $t_{\rm TI}/t_{\rm ff}$ and δ are different at different radii. We wish to study the condensation curve for localized perturbation with a given value of δ and $t_{\rm TI}/t_{\rm ff}$.

We consider localized perturbations following Section 2.3.3. The two 'stars' in Fig. 6 represent the points corresponding to the two cases where perturbations are present only at the radius of $\min(t_{\rm TI}/t_{\rm ff})$ and the radius where our homogeneous perturbation field has the maximum amplitude (≈55 kpc with background $t_{\rm TI}/t_{\rm ff} \approx 15$). We increase δ until condensation happens. For these cases of localized perturbations, $(t_{\rm TI}/t_{\rm ff})$ and δ are calculated around the radius (R_1) of maximum $\delta = \delta_{\rm max}$, within $0.99R_1$ and $1.01R_1$. The 'stars' follow a similar trend (with 10 per cent–20 per cent variation in the threshold $t_{\rm TI}/t_{\rm ff}$). Relatively, with localized perturbations it is slightly more difficult at the plane of $\min(t_{\rm cool}/t_{\rm ff})$ but slightly easier at the plane of $\delta_{\rm max}$ to condense than with perturbations throughout. But the general behaviour of the condensation curve with the changes in $t_{\rm TI}/t_{\rm ff}$ and δ (either $\min(t_{\rm cool}/t_{\rm ff})$ and $\delta_{\rm max}$ or $[t_{\rm TI}/t_{\rm ff}]_{\rm loc}$ and $\delta_{\rm loc}$) remains similar.

It is also interesting to explore the condensation curve for localized perturbations seeded in the shells outside and inside the location of $\min(t_{\rm cool}/t_{\rm ff})$. The brown and pink circles denote these runs, respectively. If we put these points according to the background $\min(t_{\rm cool}/t_{\rm ff}) = 8.18$, they will fall on the horizontal line $y = 8.18$. This line will cut the condensation curve at around $\delta \lesssim 0.1$. All the pink points correspond to amplitudes less than that, while all the brown points correspond to greater amplitude. This implies it is harder to form cold gas outside the radius of $\min(t_{\rm cool}/t_{\rm ff})$ rather than inside it. This can also be understood in terms of the entropy profile that is shallower at smaller radii (Section 3.2.2).

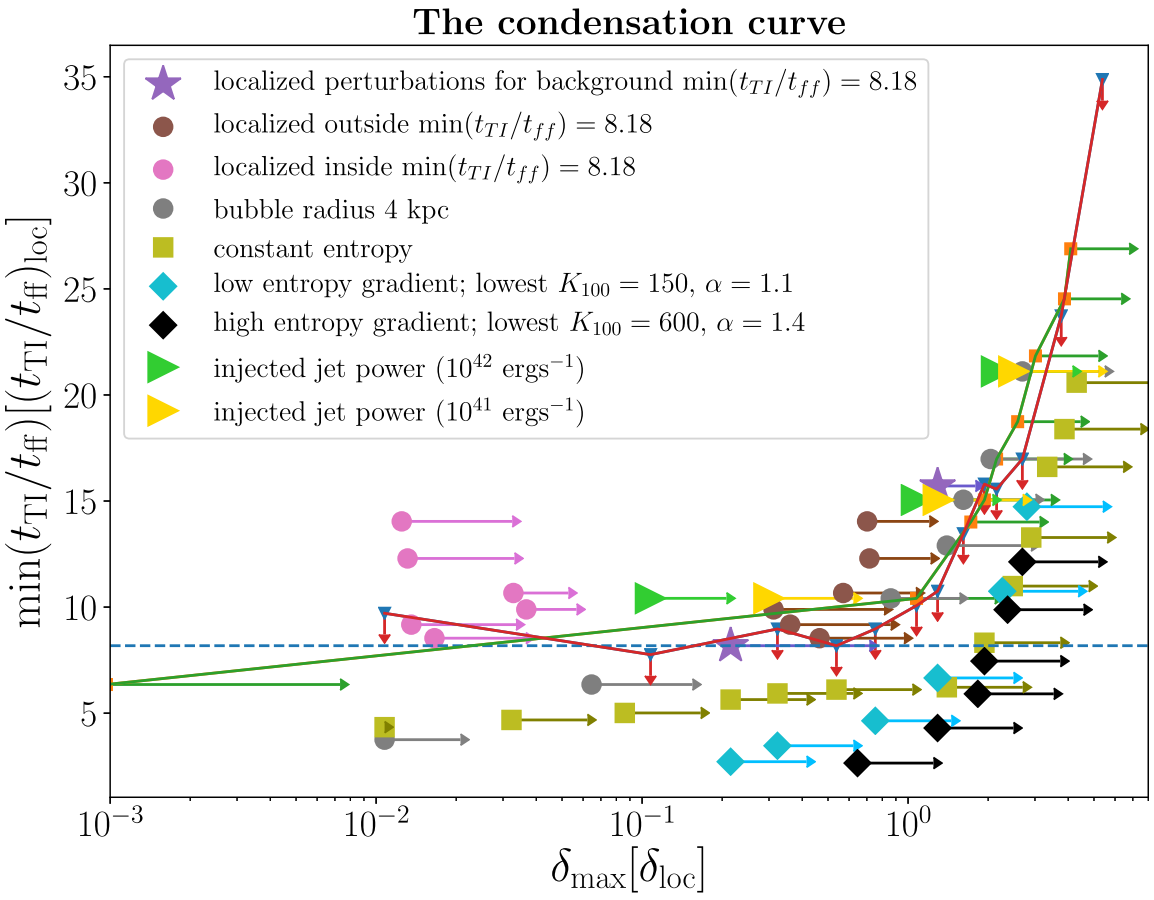

Figure 6. The condensation curve similar to Fig. 4, but with the NFW + BCG potential and varying different parameters. The red and green solid lines correspond to the runs with perturbations present throughout the cluster and form the backbone of this figure. Below this curve, the CGM is susceptible to condensation. The threshold min($t_{\rm TI}/t_{\rm ff}$) for multiphase condensation is shifted significantly for $\delta \lesssim 1$ under different conditions (jet, bubble, entropy variation). Jets enhance condensation, while buoyant bubble and steep entropy gradients suppress it. Somewhat counterintuitively, even flat entropy (throughout) systems condense out at somewhat larger amplitudes compared to the fiducial green line. For localized perturbations, there is a small scatter around the condensation curve because local entropy gradients are different in the central region and in the outskirts. Note that the two parameters ($t_{\rm TI}/t_{\rm ff}$ and δ) in the case of localized runs are calculated locally. The thin dashed line corresponds to min($t_{\rm TI}/t_{\rm ff}$) = 8.18, the background value for the runs with localized perturbations.

Note that the condensation curve for localized perturbations (marked by the local values of the parameters and shown by the pink and brown points and the 'stars' in Fig. 6) will deviate from the solid green line, which corresponds to the perturbations seeded everywhere. Fig. 8 in Singh & Sharma (2015) also shows difference in condensation of a blob inside and outside min($t_{\rm cool}/t_{\rm ff}$).

3.2.2 *Effects of a bubble and outflows*

In this section, first we plot the points corresponding to runs with perturbations throughout the domain but with a low-density bubble near the inner boundary (following Section 2.3.4). Placing the bubble near the centre, we fix the background $t_{\rm TI}/t_{\rm ff}$ while varying $\delta_{\rm max}$ to find the threshold amplitude for condensation. In Fig. 6, these are marked by the grey points with the right grey arrows. The presence of a bubble slightly enhances the $t_{\rm TI}/t_{\rm ff}$ due to low density. The effect of the bubble is more noticeable for smaller $t_{\rm TI}/t_{\rm ff}$ because the bubble mixes with the background ICM and raises the effective cooling time before cold gas condenses. So, a bubble actually prevents cold gas formation as it buoyantly rises. When min($t_{\rm TI}/t_{\rm ff}$) is high and there are large density perturbations anyway, the presence of a bubble does not make a difference and the trend follows the original condensation curve. Bigger/Smaller bubbles do not change the trend significantly.

We introduce jets of constant power into an identical ICM set-up (following Section 2.3.6). The jets enhance cold gas formation as we observe condensation for smaller perturbation amplitudes. For two different jet powers $\approx 10^{41}$ erg s^{-1} and $\approx 10^{42}$ erg s^{-1} (varying $\dot{M}_{\rm acc}$), we have three runs each corresponding to different initial min($t_{\rm TI}/t_{\rm ff}$) (given by the lime-green and golden right triangles in Fig. 6), where we see that with higher jet power it is mildly easier for cold gas to condense. Precisely, for the lowest min($t_{\rm TI}/t_{\rm ff}$), the threshold δ required is three times higher than that with higher jet power. Our jet injection increases the local density contrast of the CGM, rather than heat it, thereby making multiphase condensation easier.

3.3 NFW + BCG: background entropy variation

For the next three cases (the light green, blue, and black squares in Fig. 6), we initialize the ICM with a constant entropy and a radially varying power-law entropy, respectively (Section 2.3.5). We try the second case for two different entropy gradients (blue: lower gradient, $\alpha = 1.1$; black: higher gradient, $\alpha = 1.4$). For the first

Table 2. Numerical experiments to quantify the amount and extent of cold gas for different entropy profiles. We use the following parameters for all the runs: $\delta_{max} = 0.2$, $n_{e,out} = 0.035\,cm^{-3}$ and each run corresponds to $0.65q_{thresh}$.

Entropy	$\min(t_{TI}/t_{ff})$ (q_{thresh}; compare with Fig. 6) at $\delta_{max} = 0.2$	$\min(t_{TI}/t_{ff})$ ($0.65q_{thresh}$)	Location of $\min(t_{TI}/t_{ff})$ (in kpc)	Average cold mass ($M_\odot$)	$r_{cold,max}$ (kpc)
K_0K_{100}	9.8	6.4	17.3	2.55×10^8	15.26
K_0	6.0	3.9	99.09	1.75×10^9	75.66
K_{100}	3.88	2.5	1.009	1.56×10^7	10.84

Note. r_{max} is the maximum radius upto which cold gas is obtained for all times. Note that q_{thresh} for each of these cases fall almost on top of the condensation curves, respectively, in Fig. 6, which implies $n_{e,out}$ does not affect the curve.

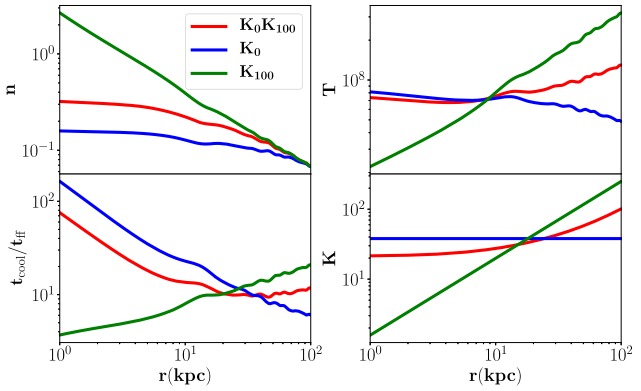

Figure 7. The radial profiles for runs with different entropy profiles (K_0K_{100}, K_0, and K_{100}) at the threshold for condensation ($q_{thresh} = \min[t_{TI}/t_{ff}]$) for $\delta_{max} = 0.2$. These three cases are considered for the comparisons we do in Section 3.3.1. All these runs have $n_{e,out} = 0.035\,cm^{-3}$. Although density profiles are very different, the total gas mass (which is dominated by the largest radii) is very similar for the three cases.

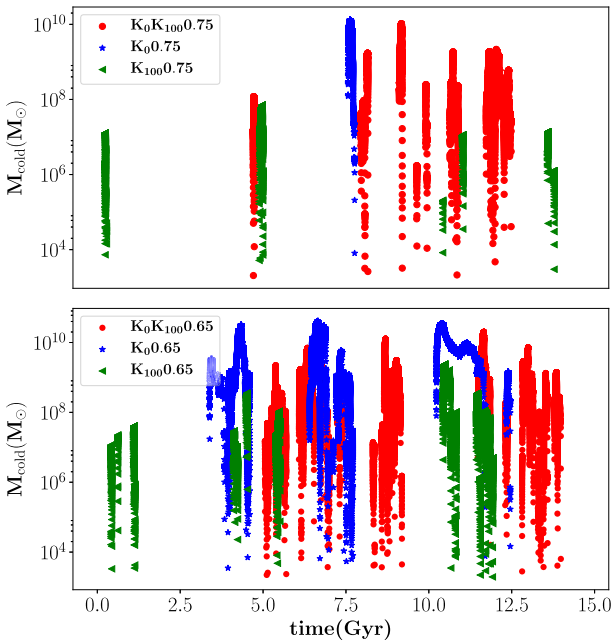

Figure 8. The total cold gas mass as a function of time for different entropy profiles (K_0K_{100}, K_0, and K_{100}) with 0.75 and $0.65q_{thresh}$ where $q = \min(t_{TI}/t_{ff})$. Total gas condensing out increases as we move into the condensation zone (0.75–$0.65q_{thresh}$). Additionally, for K_0 the total amount of cold gas grows faster than for K_0K_{100} and K_{100}, which further implies that larger cores give rise to enhanced condensation inside the condensation zone.

case, the threshold condensation curve is slightly lower compared to the fiducial curve that has both an entropy core and a power law in the outskirts. This implies that it is more difficult to condense in this regime. However, with constant background entropy we also see that once condensation is triggered, there is a large amount of gas condensing out of the hot medium. We discuss this further in the next section. The runs with large positive entropy gradients form cold gas at a much higher threshold amplitude, which is raised a little more for a larger gradient. Beyond $\delta \gtrsim 1$, the condensation curve converges for all the cases and provides substantial evidence that once the ICM has a very large density perturbation, it will start forming cold gas essentially irrespective of the background t_{TI}/t_{ff}.

3.3.1 Amount of cold gas with entropy variation: implications for the CGM

Because of numerical problems at the outer boundary with a realistic density, we have runs with constant entropy throughout in which we have increased $n_{e,out}$ (Section 2.2.2). We need to assure that the condensation curve is not affected due to a different outer density. Hence, we test cases with different entropy profiles but using this new outer density. We compare three cases with different profiles: one with a constant inner entropy and outer power law (K_0K_{100}), one with a constant entropy throughout the medium (K_0), and one with power-law entropy ($\alpha = 1.1$, see Section 2.1.2) throughout the medium (K_{100}). For all the runs, we keep the outer boundary at $n_{e,out} = 0.035\,cm^{-3}$. We fix the maximum amplitude $\delta_{max} = 0.2$ and scan across a range of background $\min(t_{TI}/t_{ff})$ to see up to what threshold value of this parameter (second column in Table 2) we see condensation. The radial profiles for the backgrounds with the threshold t_{TI}/t_{ff} that just show cold gas are shown in Fig. 7. The corresponding points for K_0K_{100} and K_{100} coincide with the ones shown in the respective condensation curves (match the values in the second column of Table 2 with Fig. 6 for $\delta_{max} = 0.2$). This way we verify that the outer density does not affect the condensation curve.

We also consider these three cases to compare the amount of cold gas produced in each case. For that, we do a few numerical experiments keeping the same amplitude of perturbation ($\delta_{max} = 0.2$) and lower the $q = \min(t_{TI}/t_{ff})$ below the threshold (q_{thresh}), that is, we move into the condensation zone. We try three different entropy profiles with 0.75, 0.7, and $0.65q_{thresh}$, respectively. Fig. 8 shows the total cold gas mass as a function of time in the runs with 0.75 and $0.65q_{thresh}$. As expected, we see an increase in the cold gas mass as we move into the condensation zone. The cases with large cores give maximum cold gas inside the condensation zone. The cases with $0.7q_{thresh}$ follow a similar trend. The maximum radial

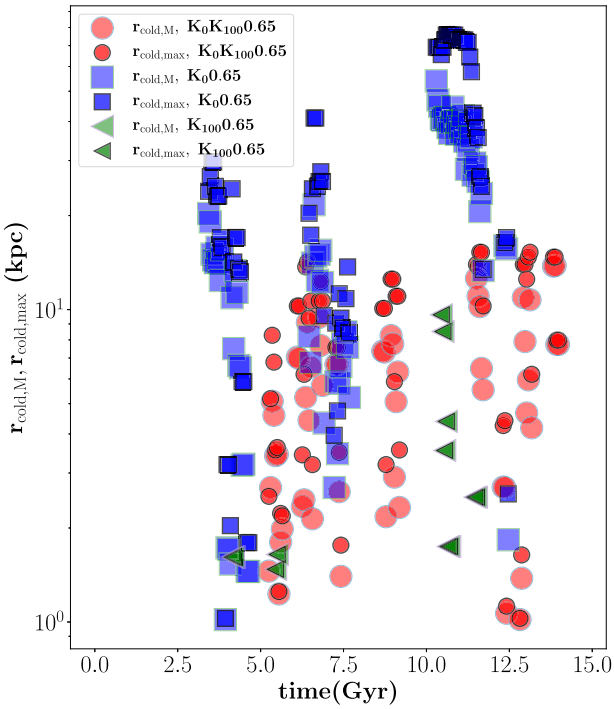

Figure 9. The radius of cold gas (r_{cold}) as function of time for the three entropy profiles K_0K_{100}, K_0 and K_{100} with $0.65q_{thresh}$, where $q = \min(t_{TI}/t_{ff})$. The bigger circles/squares/triangles represent the mass averaged radius of the cold gas ($r_{cold,M}$; eq 13) and the circles/squares/triangles with black border correspond to the maximum radius where cold gas is present ($r_{cold,max}$). Note that in K_{100}, $r_{cold,M}$ and $r_{cold,max}$ are coincident.

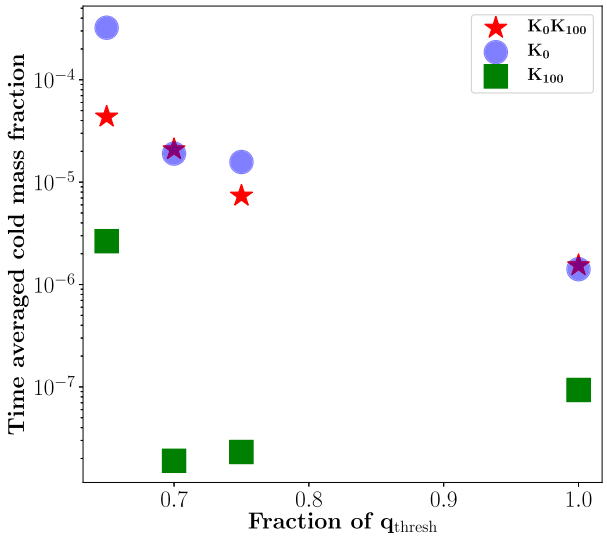

Figure 10. The time-averaged (over the entire 15 Gyr) cold gas mass for different entropy profiles (K_0K_{100}, K_0, and K_{100}) as a function of q_{thresh}, $0.75q_{thresh}$, $0.7q_{thresh}$, and $0.65q_{thresh}$ where $q = \min(t_{TI}/t_{ff})$. This shows that on an average the run K_0 starts condensing larger amount of cold gas and this is also true deeper into the condensation zone. Note that the amount of cold gas for the power-law entropy profile (K_{100}) at $0.65q_{thresh}$ is comparable to the other cases (K_0, K_0K_{100}) at $q_{thresh} = 1$ and the rise in the mass fraction is maximum for a flat entropy profile.

extent up to which cold gas is seen in K_0 is also the largest as shown in Table 2, which also gives the amount of cold gas averaged over the entire time. This implies that for the CGM (which have larger cores), TI models predict a higher amount of cold gas spread over larger radii. Fig. 9 shows the mass-weighted cold gas radius (r_{cold}) and the maximum cold gas radius as functions of time. We calculate mass-weighted r_{cold} as

$$r_{cold,M} = \int r_{cold} dM_{cold} / \int dM_{cold}. \quad (13)$$

Fig. 10 shows the gas mass fraction averaged overtime for backgrounds with different fractions of q_{thresh}. The amount of cold gas in the run with entropy gradient is much smaller compared to the other two (flat entropy, core + power-law entropy) cases. Not only is the mass of the cold gas lower, but the rate of increase of the cold gas mass with a decrease in q (a fraction of q_{thresh}) is also smaller for this case.

4 DISCUSSION AND ASTROPHYSICAL IMPLICATIONS

4.1 Significance of the condensation curve

The condensation curve defines a zone of condensation in an idealized parameter space corresponding to any CGM environment. We do not quantify in detail how much gas condenses out (except in Figs 8 and 10) within the condensation zone and whether it is sufficient for star formation. Instead, we simply delineate the parameter space for which multiphase condensation occurs due to TI. It is likely that more cold gas will be formed away from the condensation curve into the zone of condensation (Fig. 8). For $\delta_{max} \lesssim 1$ ($\delta_{min(t_{cool}/t_{ff})} < \delta_{max}$), valid for cool core clusters, the threshold value of background $\min(t_{cool}/t_{ff})$ plays a pivotal role in determining whether multiphase condensation is possible. This corroborates earlier works that consider small, isobaric perturbations. The interesting feature of the condensation curve is that it steeply rises beyond the amplitude of $\delta_{max} \sim 1$. This makes it evident that high-amplitude perturbations trigger condensation, almost irrespective of the ratio of the background t_{cool}/t_{ff}. The relevance of a threshold $\min(t_{cool}/t_{ff})$ of the background medium loses significance in this regime. This may explain the cold gas formation for the backgrounds with $\min(t_{cool}/t_{ff})$ ratio as high as 15−30 (Hogan et al. 2017). However, note that cold gas can last longer if it has angular momentum and the ICM can be seen in a state of $\min(t_{cool}/t_{ff}) \gtrsim 10$ even if the cold gas originated in a state with the core lying below the threshold $\min(t_{cool}/t_{ff}) \lesssim 10$ (Prasad et al. 2015, 2018).

The location of the large density contrast is also important for the susceptibility to condensation. From our localized perturbation runs, it is evident that inside the region of $\min(t_{cool}/t_{ff})$, close to the centre, condensation occurs even for locally high values of t_{cool}/t_{ff} (of course $\min(t_{cool}/t_{ff})$ is still smaller than the threshold). The ease of condensation closer to the centre can be interpreted as a consequence of the shallower entropy gradient. Interestingly, for a constant entropy throughout the medium, the threshold $\min(t_{TI}/t_{ff})$ is smaller than that in core + power-law entropy profile, however, the quantity of gas that condenses out is significantly large and distributed over large radii.

We plot a modified version of the condensation curve in Fig. 11 in which we take the condensation curves for NFW and NFW + BCG and label the perturbation amplitude by $\delta_{rms}(r)$ averaged around the radius (H) of $\min(t_{cool}/t_{ff})$ between $0.9H$ and $1.1H$. We do a simple analytic estimate to understand the condensation curve. For a single blob moving through the medium, we know that the ratio

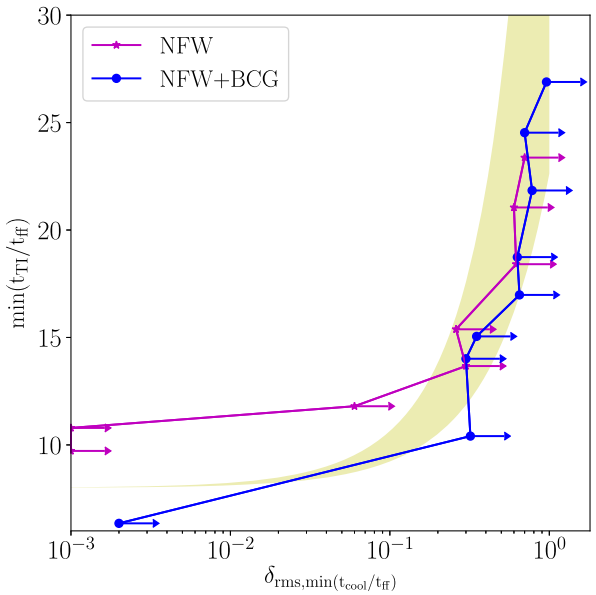

Figure 11. The condensation curve using the average $\delta_{rms}(r)$ ($\lesssim$local δ_{max}; see the red lines in Fig. 3) between $0.9H$ and $1.1H$, where H is the location of $\min(t_{cool}/t_{ff})$ in each run. The region shaded in yellow corresponds to t_{cool}/t_{ff} of the blob between $\alpha_c = -1$ and $\alpha_c = 0.5$ as described in equation (14) that provides a good description of the condensation curve derived from our simulations.

of the cooling time to the free-fall time in a background of density n_0, temperature T_0, $t_{cool}/t_{ff} = \left(t_{cool}/t_{ff}\right)_0$, and density contrast δ between the blob and the background can be expressed as

$$\left(\frac{t_{cool}}{t_{ff}}\right)_{blob} = \frac{\frac{3}{2}n_{blob}k_B T_{blob}}{n_{blob}^2 \Lambda(T_{blob}) t_{ff,blob}} = \left(\frac{3}{2}\frac{k_B}{n_{blob}T_{blob}}\right)\frac{T_{blob}^2}{\Lambda(T_{blob})t_{ff,blob}}.$$

Now, we consider that the blob is in pressure equilibrium with the medium and hence $n_0 T_0 = n_{blob} T_{blob}$ (this is justified because sound-crossing time is short). Therefore, we can simply write $T_{blob} = T_0/(1+\delta)$. At a given radial location, the free-fall times for the blob and the background are the same: $t_{ff,blob} = t_{ff,0}$. We also consider a simple form of the cooling function as $\Lambda(T) = \Lambda_0 T^{\alpha_c}$ and obtain the following expression:

$$\left(\frac{t_{cool}}{t_{ff}}\right)_{blob} = \left(\frac{3}{2}\frac{k_B}{n_0 T_0}\right)\frac{T_0^2/(1+\delta)^2}{\Lambda_0 T_0^{\alpha_c}/(1+\delta)^{\alpha_c} t_{ff,0}} = \left(t_{cool}/t_{ff}\right)_0 (1+\delta)^{(\alpha_c - 2)}. \quad (14)$$

The yellow shaded region in Fig. 11 shows the parameter space corresponding to $(t_{cool}/t_{ff})_{blob} = 8$ and the varying parameters being $(t_{cool}/t_{ff})_0$ and δ between the values of $\alpha_c = -1$ (crudely mimicking galaxy cooling function) and $\alpha_c = 0.5$ (cluster cooling function). This simply shows that the condensation curve traces out the locus of $\left(\frac{t_{cool}}{t_{ff}}\right)_{blob} = 8$, i.e. multiphase condensation in the plane of background $\min(t_{cool}/t_{ff})$ happens such that the perturbations (rather than the background) maintain a threshold (t_{cool}/t_{ff}). Hence, we generalize the idea that the background $\min(t_{cool}/t_{ff})$ must fall below a threshold for multiphase condensation, to the (t_{cool}/t_{ff}) of the overdense region.

Multiphase condensation may not always happen in the ICM and CGM when the background $\min(t_{TI}/t_{ff})$ is high. Recent X-ray observations such as Werner et al. (2018) discuss the existence of red nugget galaxies, which are the building blocks for compact, massive galaxies at the current time and which have no recent star formation. One such system, Mrk 1216, has very short cooling times and small core entropy, which suggests that gas in the galactic core should condense out of the medium. But, with deeper gravitational potential, the $t_{cool}/t_{ff} \approx 20$ is somewhat high and it does not show any signatures of recent condensation. Such systems, unlike the standard cool-core clusters (Pulido et al. 2018), can distinguish t_{cool}/t_{ff} models from those based on just t_{cool} or the core entropy. Since haloes grow hierarchically due to gravity, the t_{ff} profiles are rather similar for typical haloes. But these galaxies with unusual growth histories can be good testbeds to understand multiphase condensation in haloes.

4.1.1 The condensation curve with t_{TI}/t_{BV}

An important time-scale, which characterizes the linear response of isobaric density/entropy perturbations in a stratified atmosphere, is the Brunt–Väisälä time-scale defined as

$$t_{BV} \equiv \left[\frac{g}{\gamma}\frac{d}{dr}\ln\left(\frac{p}{\rho^\gamma}\right)\right]^{-1/2}, \quad (15)$$

where we use the background pressure and density profiles. It is useful to see how the condensation curve looks like if we use t_{TI}/t_{BV} instead of t_{TI}/t_{ff} to quantify the susceptibility to condensation. Fig. 12 shows the time-scale ratios, t_{TI}/t_{BV} and t_{TI}/t_{ff}, for different cases (at $t \approx 0$ with and without perturbations, and at the onset of multiphase condensation, $t \approx t_{onset}$). For one, it is straightforward to calculate t_{ff} (and hence t_{TI}/t_{ff}) unlike t_{BV} because the angle-averaged entropy profiles with perturbations have sharp jumps and negative radial derivatives at some points (especially where the atmosphere is close to isentropic). Since $\min(t_{TI}/t_{BV})$ appears to be a factor of $\sim$2 lower than $\min(t_{TI}/t_{ff})$ in Fig. 12 at the onset of multiphase condensation, we expect the condensation curve (Fig. 6) based on $\min(t_{TI}/t_{BV})$ to be shifted downwards by a factor of $\sim$2 compared to the curve with $\min(t_{TI}/t_{ff})$.

Fig. 12 also shows that even if the initial background has a large t_{TI}/t_{ff}, the perturbation level (required at the threshold of condensation) is such that the t_{TI}/t_{ff} remains around $\sim$10 (see the thick dashed lines), which is consistent with our phenomenological model presented in Section 4.1 that argues that an overdense blob leads to multiphase gas if its $t_{TI}/t_{ff} \lesssim 10$, even if the background has a higher ratio.

4.2 Role of entropy gradient in condensation

Voit et al. (2017) gives significant emphasis on the role of entropy gradient in regulating feedback. According to their model, cold gas can condense out in two regions via different mechanisms: in the central isentropic zone due to TI and due to uplift in the outer zones with a steeper entropy profile. The authors argue that the power-law entropy zone plays a crucial role in the cool core feedback cycles. We confirm that multiphase condensation is harder and less widespread with steeper entropy profile. Fast buoyancy oscillations are expected to damp the linear growth of multiphase condensation once the perturbations become larger. In the absence of buoyancy oscillations, condensation should be easy. But contrary to the expectations from linear theory, the constant entropy models require a smaller value of the threshold $\min(t_{TI}/t_{ff})$ for condensation compared to the core + power-law profile (making the onset of condensation appear more difficult; see Fig. 6). The reason for this

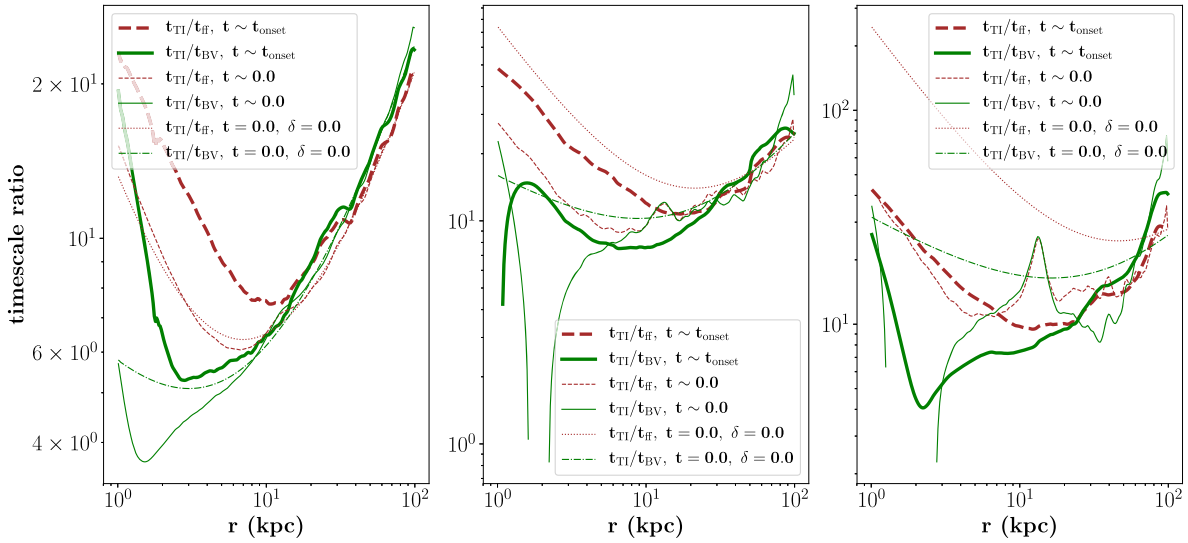

Figure 12. The time-scale ratios, t_{TI}/t_{ff} and t_{TI}/t_{BV}, with radius for three different initial min(t_{TI}/t_{ff}) (6,14,25, without perturbations, from left to right; the corresponding min[t_{TI}/t_{BV}] are 5, 10, 16) with NFW + BCG runs from the condensation curve in Fig. 6 ($\delta_{max} \sim 0.001$, 1, 3) and Fig. 11 ($\delta_{rms} \sim 0.001$, 0.3, 0.6). All the radial profiles (except ones with $\delta = 0.0$) are time-averaged within a 0.5 Gyr time window. We use a fifth-order polynomial fit to smoothen the entropy profile and then take the derivative to obtain t_{BV}. Notice that the profiles with perturbations have regions where t_{BV} is not defined as the background entropy gradient is negative. The range of min(t_{TI}/t_{ff}) close to the onset is in the range 7–10 and min(t_{TI}/t_{BV}) is in the range 4–7.

is the long cooling time for this case relative to the run-time (the cooling time at the location of min[t_{TI}/t_{ff}] is much shorter for a rising entropy profile). As the condensation sets in, it is relatively more widespread in the constant entropy model. However, buoyancy oscillations and the absence of multiphase gas are not always coincident in this case across the entire run-time. This implies that strong buoyancy oscillations are sufficient but not always necessary to prevent multiphase condensation.

4.2.1 *Implications of shallower entropy profile in the CGM*

A large fraction of the CGM in smaller mass haloes is expected to be within the location of min(t_{cool}/t_{ff}) (or in other words, expected to have large isentropic cores; Maller & Bullock 2004; Sharma et al. 2012b), and hence multiphase condensation is expected to be more widespread. For our runs with constant entropy throughout the medium, the location of min(t_{cool}/t_{ff}) is pushed almost up to the outer boundary. These runs mimic a CGM-like atmosphere with a large radial extent of the central core. The threshold min(t_{cool}/t_{ff}) required for multiphase condensation in these runs, is, in fact, less than the ones that have a power-law entropy profile in the outskirts. But, we observe that once condensation is triggered, there is a large amount of gas cooling out of the background medium and over a large radial extent (see Figs 8 and 9). This may explain the observation (Tumlinson et al. 2017) of cold gas along most lines of sight through the CGM. However, for a CGM, the background medium is not necessarily in global thermal balance, particularly for reasonably small halo masses. Thus, our results should be taken to be qualitative but robust indicators.

In our runs, the medium with constant entropy has relatively more condensed gas and is clearly more disrupted than the other two entropy profiles if we see the cores at one of the times of peak activity. Fig. 13 shows the number density maps for all the cases at one of these times, which are not necessarily coincident. For K_0, the low-density hot bubbles generated in the central region (produced because of our heating prescription) can move out up to large radii freely, due to the lack of buoyant oscillations. Consequently, such bubbles grow and perturb the gas at large radii. We see distinct filaments spreading up to ∼40−50 kpc and gas condenses out along these. For the core + power-law entropy profile, cooling and heating are confined within smaller radii. In the pure power-law profile, the cooling and disrupted phase of the gas remains more tightly confined than the former.

For the CGM, it has been theoretically predicted that the virial shock can be unstable for significantly lower mass haloes (Birnboim & Dekel 2003). Dense streams can enter the halo (Kereš et al. 2005) providing large overdensities that may seed multiphase condensation. Observations of metal-rich cold gas in the outskirts by COS–Haloes observations seem to imply that the cold clumps seen along all lines of sight are recycled by feedback (Werk et al. 2013; Ford et al. 2016). However, we cannot rule out the possibility of large perturbations seeded by relatively pristine dense streams (of course the local IGM is polluted by outflows at much earlier era). Dense ram pressure stripped gas from satellite galaxies orbiting massive groups and clusters (Yun et al. 2019) may seed large overdensities in the hot medium. Molecular gas has been observed to be in the stripped tail of such galaxies (Jáchym et al. 2017). Magnetic fields can also aid multiphase condensation by providing magnetic support against gravity and thus seeding large density perturbations (Ji, Oh & McCourt 2018).

4.2.2 *How do the entropy profiles evolve?*

While it is most convenient to plot the condensation curve (Fig. 6) in terms of the background unperturbed value of min(t_{TI}/t_{ff}), the background shell-averaged profiles (and hence t_{TI} and t_{BV}) change with perturbations and in time (see Fig. 12). Voit et al. (2017, 2018) argue that buoyancy oscillations are driven by TI, and the density fluctuations saturate when the buoyancy damping rate balances the growth rate; i.e. $t_{TI} \sim t_{BV}$. Another possibility for saturation, especially for shallow entropy gradients, is obtained via balancing t_{TI} and the turbulent eddy turnover time (McCourt et al. 2012;

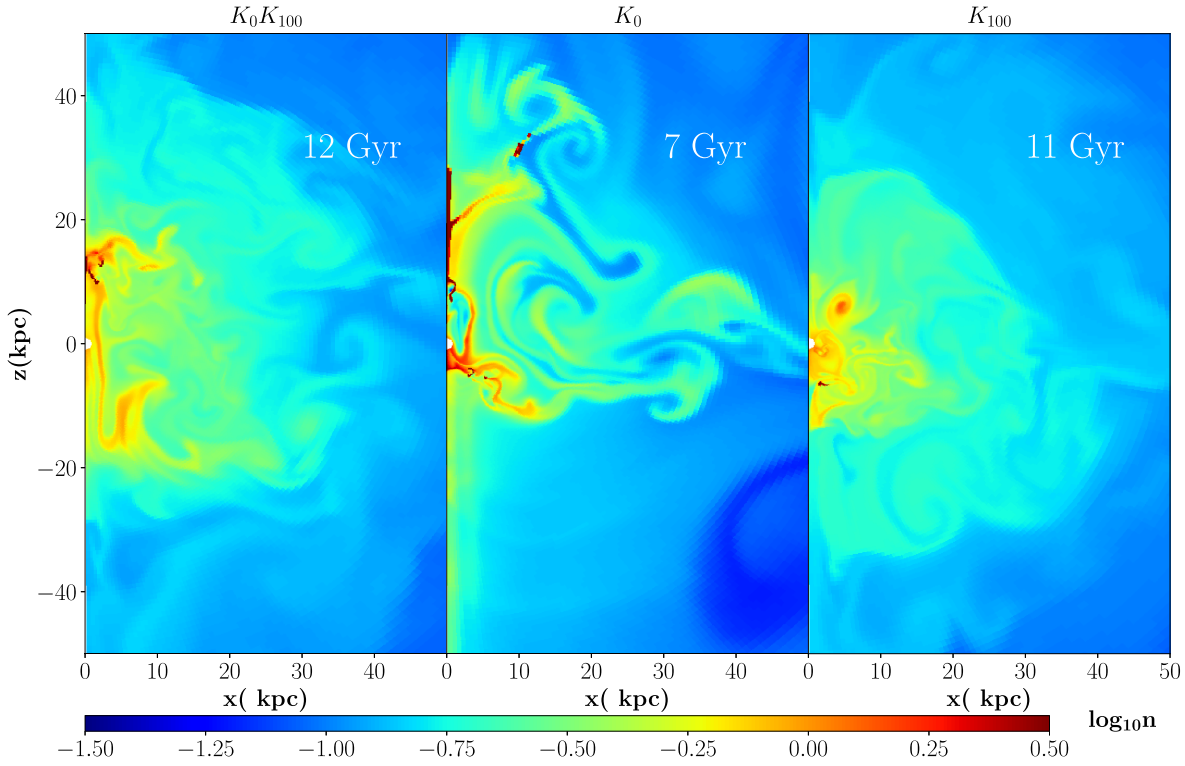

Figure 13. The number density snapshots for the three different entropy profiles K_0K_{100}, K_0, and K_{100}, for $0.65q_{\rm thresh}$ at one of the times when the cores have extended cold gas. For K_0, gas condenses out along dense filaments distributed over a much larger region compared to the other two cases. In axisymmetric simulations using spherical coordinates, there is a tendency of cold gas to accumulate close to the poles for some time, as seen here. However, multiphase gas originates away from the poles and our key results are robust.

Singh & Sharma 2015). We note that our initially isentropic runs (K_{100}) develop a mild positive entropy gradient before the onset of condensation. It appears unlikely that the weak entropy gradient in these cases plays a significant role. However, our results with larger entropy gradient runs strongly suggest that a steep entropy gradient suppresses condensation.

It is useful to understand the entropy evolution of different background profiles with and without heating/cooling. We perform some of the runs in Table 2 to characterize how entropy profile is modified without heating and cooling. All these runs show a small increase in the central entropy (due to the dissipation of gravity waves) and no entropy sorting. When cooling and heating are included, core + power law and constant power-law runs (K_0K_{100} and K_0) show the entropy becoming smaller in the central region as the lower entropy material at larger radii moves in (i.e. entropy sorting), which implies that entropy sorting is caused by cooling and heating. For a power-law profile (K_{100}), the central entropy increases rather than decreasing. After significant condensation, all thermal balance simulations seem to approach a similar entropy profile in the core (compare figs 5 and 7 in Sharma et al. 2012a), which can be understood from the tendency of such atmospheres to become marginally susceptible to multiphase condensation in the core.

Fig. 14 shows the distribution of entropy in shells for the three cases (K_0K_{100}, K_{100}, K_0 including cooling/heating) at the onset of cold gas. The solid coral lines show the medians, and the dashed coral lines enclose the regions within 20–80 percentile, and the symbols indicate the entropy distribution of individual grid cells. This figure demonstrates several important aspects of entropy evolution. First, the extreme low-entropy region is spread out till very large radii for the flat entropy run (K_0), somewhat less in K_0K_{100} and the least in K_{100}. This radial extent of cold and hot gas is within the location of $\min(t_{\rm TI}/t_{\rm ff})$ in all the three cases. Secondly, the outskirts in K_0 have a larger spread in entropy compared to the central regions, contrary to K_0K_{100} and K_{100}. This implies that despite the sorting of entropy in the central region (enhanced entropy gradient) for K_0, multiphase condensation starts in the outskirts. Thirdly, the entropy is typically higher in K_0 than the central regions of K_0K_{100} and K_{100} despite the condensation of a larger amount of cold gas in the former. This sums up how it is easier to obtain significant cold gas in a constant entropy environment similar to the CGMs in which a larger volume is susceptible to multiphase condensation.

4.3 Role of outflows and bubbles in condensation

Active galactic nuclei (AGN) jets can promote multiphase condensation in two ways: their trails entraining gas from the core and in case of supersonic jets, impinging into the medium and compressing regions in which density is enhanced. In our set-up, there are overdense regions seeded already and the gentle outflows that we have can simply entrain the gas. We inject low jet powers (and thermal balance in shells) so perturbations can become denser due to entrainment and there is an onset of condensation with a smaller amplitude than what is predicted by the background condensation curve. With an injection of higher jet powers, it is relatively easier to obtain cold gas, particularly for a small background $t_{\rm cool}/t_{\rm ff}$ (comparing the lime-green and golden right triangles in Fig. 6). However, it is worth mentioning that extremely powerful jets heat

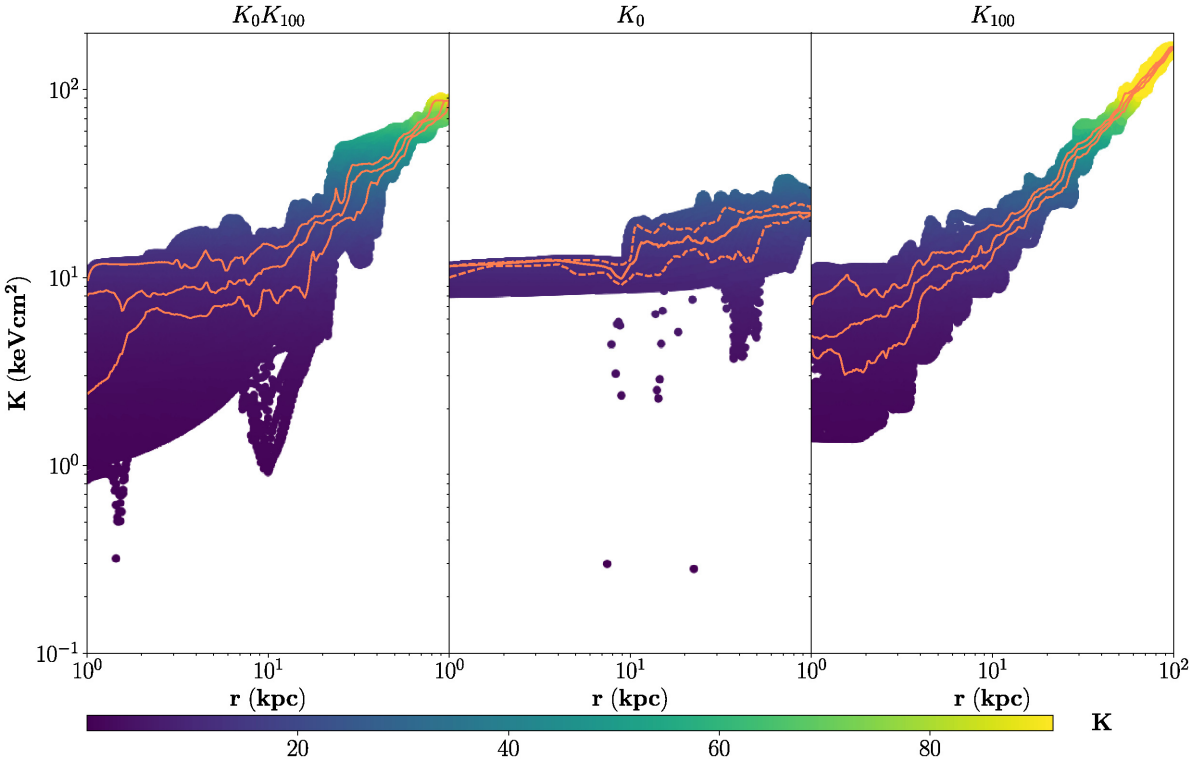

Figure 14. The entropy distribution (across θ-direction) of all grid points in a given radial shell for K_0K_{100}, K_0, and K_{100} runs at the onset of condensation with the colour bar showing the entropy on a linear scale. The coral solid lines show the median entropy profile at each radius and the coral dashed lines enclose the regions between 20 and 80 percentile.

up the core on an average and the core has lower density for very long times (Prasad et al. 2015). In such a case, the total amount of cold gas (in an average sense) decreases in the system. In our set-up, condensation becomes difficult for supersonic jets due to overheating.

Contrary to the jets, we observe that our buoyant bubbles have a negative impact on condensation. The bubble is disrupted after moving a small distance away from the centre. But it prevents condensation particularly for small values of background min($t_{\rm cool}/t_{\rm ff}$), reducing this threshold to lower values for same amplitudes, compared to what is expected from the condensation curve. Revaz, Combes & Salomé (2008) show condensation occurring in the wake of large-scale bubbles in their ICM simulations. However, the background ICM in these simulations, is not in thermal equilibrium, with a cooling flow occurring in a few hundred megayears. Without any heating source, the overdensities in the wake of the bubble can condense out easily given enough time. In fact, these simulations were run for only 600 Myr and the minimum cooling time was around 400 Myr. The cooling catastrophe can dominate in a few hundred Myrs for this case and most of the gas will cool down to very low temperatures even without a bubble. Our set-up is qualitatively different because of the presence of heating (which we implement in the form of idealized thermally balanced shells).

Thus, while jets are conducive to condensation of reasonably large density perturbations, bubbles suppress the condensation. However, the magnitude of the effect is mild and does not affect the background condensation curve to a great extent. A thorough exploration of the entire parameter space of bubbles and jets is beyond the scope of this work.

5 CONCLUSIONS

We carry out a suite of simulations to explore the factors that affect multiphase condensation in the CGM. Earlier simulations (McCourt et al. 2012; Sharma et al. 2012a) considered only small-amplitude perturbations in the ICM in hydrostatic and global thermal balance. They find that min($t_{\rm cool}/t_{\rm ff}$) in the background medium plays a pivotal role in determining whether multiphase condensation happens. While Sharma et al. (2012a) put a threshold (≈10) for cold gas to form, which is corroborated by subsequent observations and simulations, Choudhury & Sharma (2016) explored the possibility of slightly higher values of threshold min($t_{\rm cool}/t_{\rm ff}$) for somewhat different potentials and find that it can vary within a factor of 2. Recent observations hint at multiphase medium for background $t_{\rm cool}/t_{\rm ff}$ as high as ≈25 (Hogan et al. 2017). This partly motivates our investigation of the possible conditions under which a medium, with large background min($t_{\rm cool}/t_{\rm ff}$), can be susceptible to multiphase condensation. Our numerical experiments reveal that theoretically, it is always possible to condense gas out of the hot medium if the initial density inhomogeneities are large enough (Pizzolato & Soker 2005; Singh & Sharma 2015). Such large density perturbations can be due to dense regions formed around low-density AGN-driven bubbles, stripping of dense gas from galaxies moving through the CGM, cosmological cold filaments breaking up as they enter the virial radius, etc.

The main conclusions of our work are the following:

(i) **The condensation curve:** We introduce a condensation curve in the min($t_{\rm TI}/t_{\rm ff}$) − $\delta_{\rm max}$ plane, which defines the regime in which multiphase condensation occurs in the ICM/CGM. This curve also shows that below an amplitude $\delta_{\rm max} \approx 1$ ($\delta_{\rm min(}t_{\rm cool}/t_{\rm ff}{\rm)} < \delta_{\rm max}$), it is

the $t_{\rm TI}/t_{\rm ff}$ ratio of the background atmosphere that governs condensation. For large perturbation amplitudes, the condensation curve rises steeply, implying that the background $t_{\rm TI}/t_{\rm ff}$ has a relatively small role to play. On the contrary, the $t_{\rm TI}/t_{\rm ff}$ *of the condensing blob* is what plays a crucial role in determining multiphase condensation. The condensation curve corresponds to the threshold $t_{\rm cool}/t_{\rm ff}$ *of the blob* $\sim$10 irrespective of the background (see Section 4.1 and equation 14). We anticipate the condensation curve to shift downwards by a factor of $\sim$2, if defined in terms of $\min(t_{\rm TI}/t_{\rm BV})$ (see Section 4.1.1). It will be useful to create a similar condensation curve relative to the turbulent velocity (say in the $\min[t_{\rm TI}/t_{\rm ff}]$–turbulent velocity plane) because turbulence cannot only produce density fluctuations (Zhuravleva et al. 2014; Mohapatra & Sharma 2019) but can also directly affect the physics of multiphase condensation (Voit 2018). We delineate the susceptibility of the medium to produce multiphase condensation but do not quantify in detail the amount of cold gas formed. However, the zone of condensation is below this curve and we show that we get more cold gas if we move away from the condensation curve into this zone.

(ii) **Localized perturbations slightly deviate from the curve but follow the trend:** The condensation curve is defined by labelling our runs with the background $\min(t_{\rm TI}/t_{\rm ff})$ and the maximum value of the amplitude of density perturbations (δ). However, δ and $t_{\rm cool}/t_{\rm ff}$ (or $t_{\rm TI}/t_{\rm ff}$) vary spatially. Local condensation depends on the local values of these parameters. In order to understand how the radial location of overdensity affects multiphase condensation, we seed perturbations only in narrow radial shells. These tests show that the amplitude of perturbations required for condensation, in case of localized perturbations, is close to what we expect from the condensation curve. As one moves out from the radius of $\min(t_{\rm TI}/t_{\rm ff})$, it is harder to get cold gas because the local $t_{\rm cool}/t_{\rm ff}$ is large. However, note that outside the radius of $\min(t_{\rm TI}/t_{\rm ff})$, condensation in local patches (the brown points in Fig. 6) follows the locus of $\left(\frac{t_{\rm cool}}{t_{\rm ff}}\right)_{\rm blob} \lesssim 10$. As one moves inwards from the radius of $\min(t_{\rm TI}/t_{\rm ff})$, condensation is relatively easier.

(iii) **Effect of entropy variation on the condensation curve:** We test the effect of entropy gradient by initializing some simulations with only constant entropy and some with power-law entropy. A constant entropy lowers the threshold $\min(t_{\rm TI}/t_{\rm ff})$, implying that the onset of condensation is somewhat difficult compared to the core + power-law entropy profile. This is because the constant entropy runs have only been run for a small number of cooling times because $\min(t_{\rm cool})$ is the longest. However, once condensation happens in this case, it is more widespread. On the other hand, a large entropy gradient clearly inhibits condensation.

(a) **Implications on CGM observations:** In a medium with constant entropy throughout, it appears mildly difficult to initiate condensation as the threshold $\min(t_{\rm cool}/t_{\rm ff})$ is slightly smaller. However, for such profiles, a larger amount of gas cools out at the threshold, at much larger radii, and progressively more into the condensation zone relative to the fiducial entropy profile. The medium is disturbed up to very large radii as both hot and cold blobs move over large distances (middle panel in Fig. 13). Hence, constant entropy runs have significant implications on the observations of ubiquitous multiphase gas in the CGM as smaller mass haloes are expected to have shallower entropy profiles (e.g. see fig. 1 of Sharma et al. 2012b).

(iv) **Effect of outflows and bubbles on the condensation curve:** We investigate how the condensation curve is modified in the presence of bubbles and outflows. In our runs, we mimic a bubble by a patch of low density compared to the background. This locally increases the $t_{\rm cool}/t_{\rm ff}$ and prevents condensation. For outflows, we inject low power jets because we balance cooling and heating in shells and do not want to overheat due to energy injection by jets. This way we can compare the runs with and without outflows under similar conditions of background thermal balance. However, due to reasonably low powers, we only have gentle subsonic winds that essentially increases the density and shortens $t_{\rm cool}$ in the core. We see in our simulations that for high jet power ($\approx 10^{42}$ erg s^{-1}), the threshold amplitude of perturbations required is almost an order of magnitude less than what is expected from the condensation curve, with $\min(t_{\rm TI}/t_{\rm ff}) \approx 10$. When we decrease the jet power by a factor of 10, the threshold amplitude for the same background is three times higher. Note that this may not be a generic result for the ICM and on an average cold gas is obtained less frequently in presence of supersonic jets and AGN feedback cycles (Prasad et al. 2015) as the powerful jet events keep the core hot for a long time.

Lastly, we have tried to verify the condensation curve with a couple of 3D simulations. However, we could not carry out an exhaustive scan in the parameter space even for a single background profile because of the runs being immensely expensive. From our limited exploration, we see that the threshold $\min(t_{\rm cool}/t_{\rm ff})$ required for condensation is close to what is obtained in 2D for one of the backgrounds. We will do detailed comparisons with 3D simulations in the future.

ACKNOWLEDGEMENTS

PPC acknowledges MPA for a long-term visiting graduate fellowship. PS acknowledges an India–Israel joint research grant (6-10/2014[IC]) and a Swarnajayanti Fellowship from the Department of Science and Technology (DST/SJF/PSA-03/2016-17). PS also thanks the Humboldt Foundation that enabled his sabbatical at MPA where this work was finished. EQ was supported in part by a Simons Investigator Award from the Simons Foundation and by NSF grant AST-1715070. We thank our referee, Mark Voit, for important suggestions to improve the draft.

REFERENCES

Balbus S. A., 1988, ApJ, 328, 395
Birnboim Y., Dekel A., 2003, MNRAS, 345, 349
Bowen D. V., Chelouche D., Jenkins E. B., Tripp T. M., Pettini M., York D. G., Frye B. L., 2016, ApJ, 826, 50
Cavagnolo K. W., Donahue M., Voit G. M., Sun M., 2009, ApJS, 182, 12
Choudhury P. P., Sharma P., 2016, MNRAS, 457, 2554
Dekel A. et al., 2009, Nature, 457, 451
Fabian A. C., 1994, ARA&A, 32, 277
Fielding D., Quataert E., McCourt M., Thompson T. A., 2017, MNRAS, 466, 3810
Field G. B., 1965, ApJ, 142, 531
Ford A. B. et al., 2016, MNRAS, 459, 1745
Hayes J. C., Norman M. L., Fiedler R. A., Bordner J. O., Li P. S., Clark S. E., ud-Doula A., Mac Low M.-M., 2006, ApJS, 165, 188
Hogan M. T. et al., 2017, ApJ, 851, 66
Jáchym P. et al., 2017, ApJ, 839, 114
Ji S., Oh S. P., McCourt M., 2018, MNRAS, 476, 852
Kereš D., Hernquist L., 2009, ApJ, 700, L1
Kereš D., Katz N., Weinberg D. H., Davé R., 2005, MNRAS, 363, 2
Li Y., Bryan G. L., 2014, ApJ, 789, 153
Maller A. H., Bullock J. S., 2004, MNRAS, 355, 694
Matejek M. S., Simcoe R. A., 2012, ApJ, 761, 112
McCourt M., Sharma P., Parrish I. J., Quataert E., 2012, MNRAS, 419, 3319

Meece G. R., O'Shea B. W., Voit G. M., 2015, ApJ, 808, 43
Mohapatra R., Sharma P., 2019, MNRAS, 484, 4881
Navarro J. F., Frenk C. S., White S. D. M., 1996, ApJ, 462, 563
Nulsen P. E. J., 1997, in Soker N., ed., ASP Conf. Ser. Vol. 115, Galactic Cluster Cooling Flows. Astron. Soc. Pac., San Fransisco, p. 135
Oppenheimer B. D., 2018, MNRAS, 480, 2963
O'Sullivan E. et al., 2017, MNRAS, 472, 1482
Pizzolato F., Soker N., 2005, ApJ, 632, 821
Prasad D., Sharma P., Babul A., 2015, ApJ, 811, 108
Prasad D., Sharma P., Babul A., 2018, ApJ, 863, 62
Pulido F. A. et al., 2018, ApJ, 853, 177
Rauch M., Haehnelt M. G., 2011, MNRAS, 412, L55
Revaz Y., Combes F., Salomé P., 2008, A&A, 477, L33
Salomé P. et al., 2006, A&A, 454, 437
Sharma P., Parrish I. J., Quataert E., 2010, ApJ, 720, 652
Sharma P., McCourt M., Quataert E., Parrish I. J., 2012a, MNRAS, 420, 3174
Sharma P., McCourt M., Parrish I. J., Quataert E., 2012b, MNRAS, 427, 1219
Singh A., Sharma P., 2015, MNRAS, 446, 1895
Tremblay G. R. et al., 2012, MNRAS, 424, 1026
Tremblay G. R. et al., 2016, Nature, 534, 218
Tumlinson J., Peeples M. S., Werk J. K., 2017, ARA&A, 55, 389
Voit G. M., 2018, ApJ, 868, 102
Voit G. M., Donahue M., 2015, ApJ, 799, L1
Voit G. M., Donahue M., Bryan G. L., McDonald M., 2015a, Nature, 519, 203
Voit G. M., Bryan G. L., O'Shea B. W., Donahue M., 2015b, ApJ, 808, L30
Voit G. M., Meece G., Li Y., O'Shea B. W., Bryan G. L., Donahue M., 2017, ApJ, 845, 80
Werk J. K., Prochaska J. X., Thom C., Tumlinson J., Tripp T. M., O'Meara J. M., Peeples M. S., 2013, ApJS, 204, 17
Werner N., Lakhchaura K., Canning R. E. A., Gaspari M., Simionescu A., 2018, MNRAS, 477, 3886
Yun K. et al., 2019, MNRAS, 483, 1042
Zhuravleva I. et al., 2014, ApJ, 788, L13

This paper has been typeset from a TEX/LATEX file prepared by the author.